Effects of the electric field on the overall drop impact on a solid surface

Yu Tian [1] Zihan Peng [1] Yanchu Liu [2,*] Linsen Di [1] Ziyi Zhan [1] Dong Ye [1]
Yin Guan [3] Xinping Zhou [1] Weiwei Deng [2] and YongAn Huang [1,*]

[1]*State Key Laboratory of Digital Manufacturing Equipment and Technology,
Huazhong University of Science and Technology, Wuhan 430074, China*
[2]*Department of Mechanics and Aerospace Engineering, Southern University of Science
and Technology, Shenzhen 518055, China*
[3]*School of Energy and Power Engineering, Huazhong University of Science and Technology,
Wuhan 430074, China*

Depositing drops on a solid surface without entrapping bubbles is desirable for many spray coating and printing applications. Tian *et al.* [J. Fluid Mech. **946**, A21 (2022)] reported that an electric field can be applied to eliminate air bubble entrapments for neutral drops. Herein we provide a complete physical picture of the entire process of a drop impacting onto the solid surface under an external electric field. The electrohydrodynamic behavior during the drop impact is divided into three stages: the deformation of the drop in the electric field prior to contact, the initial contact of the drop with the substrate, and the rich postcontact phenomena including spreading, receding, jetting, and fragmentation. The results show that under the increasingly stronger electric fields, the modest drop oscillation transforms into a vertically stretched spindle. As the drop approaches the substrate, the electric stress at the south pole increases rapidly, which sharpens the bottom surface into a conical shape. The cone angle is determined by both the impact velocity and the electric field strength. After the contact, the surface electric stress tends to pull the drop upward, breaking up the drop, forming several jetting modes, and reducing the maximum spreading radius. The various drop deposition modes are summarized in a phase diagram, which sheds light on identifying appropriate electric fields for high-quality drop depositions without air bubble entrapments or jettings.

I. INTRODUCTION

The dynamics of drop impact on solid surface are of great interest to basic science as well as many emerging technologies [1–5]. For example, in inkjet printing, it is possible to produce desired shapes, structures, or three-dimensional objects by droplet deposition with computer control [6,7]. The inks can be organic/inorganic functional materials or molten metal or alloy [8–10]. To achieve high-quality printing, efforts have been made to avoid entrapping bubbles [11–13] because when a drop impacts on a solid surface, air tends to be trapped during the early contact stage (often within hundred microseconds after initial contact) [14–16]. When the thickness of the squeezed air film is $\sim 5 \mu$m, the lubrication pressure coming from the viscous stress of air flow dents the bottom of the drop into a dimple before the drop touches the substrate [17–19]. On contact, the air film is trapped by the circular receding contact line and eventually evolves into a small air bubble. The bubble size ranges from a few tens of nanometers to hundreds of micrometers, depending on the

---

*yahuang@hust.edu.cn; liuyc@sustech.edu.cn

drop diameter and Stokes number [20–24]. Researchers have proposed two strategies to eliminate the bubble entrapment: One is to reduce the ambient air pressure to weaken or eliminate the effect of air film lubrication pressure [25,26]; the other is to create microstructures on substrate surface to avoid pressure buildup in the air film [27,28]. However, neither of the two approaches is easy to implement for general purpose of printing: The reduced pressure may alter the ink evaporation, and the sealed chamber complicates the apparatus; the microfabrication is not always possible or compatible with the substrate or specific applications. Therefore, it is highly desirable to propose a more convenient method to eliminate air bubble entrapment without modifying the microstructure of the substrate surface or the inks of the drop.

Applying external forces to affect the drop impact has drawn much research interest [29–33]. For example, the introduction of magnetic fields leads to a reduced maximum spreading radius in the drop impact [34,35]. The thin air gap between the drop and substrate can be split into tunnels and subsequently squeeze the air out from the tunnels against its viscous resistance using spatially periodic dielectrophoretic force. The delicate air thin film can be fundamentally altered for even weakly charged droplets [36–38]. The impact dynamics under electric fields has also recently received extensive attention. When a drop is subject to an external electric field, there will be time-varying electrical stresses on the surface due to polarization. During the drop impact, the maximum deformation ratio, the eventual spreading radius and height, eccentricity, and other parameters of the drop can be adjusted by the external electric field [39–43]. However, the current research on drop impact under electric field is limited to single physical quantities such as droplet deformation or final spreading radius [44–46], which lacks a systematic study of the overall electrohydrodynamic (EHD) process.

Tian Yu *et al.* [47] focused on the mechanism of the external electric field on eliminating air entrapment of neutral drops deposited on the smooth rigid substrate. The competition between the bottom electric stress and the air film lubrication pressure yields the scaling of critical electric field for bubble-free depositions. However, the effect of the electric field on the subsequent spreading and receding of the drop remains unknown. Tian Ye *et al.* [48] investigated the retraction, rebound, and fragmentation of neutral drops impacting on the superhydrophobic rigid surface in an external electric field. They categorized the behaviors into four different bouncing and fracturing regimes by comparing the dynamic pressure, capillary pressure, and electrostatic pressure. Since the super-hydrophobic surface is used, the drop is prone to bounce even without electric fields, limiting the parameter window in relatively slow impacting velocities (<1 m/s). The slow velocity provides the drop with relatively long residence time compared with the capillary time, therefore, prior to contact, the drop undergoes dramatic stretching and deformation, which may affect the impact outcome.

The survey of literature shows that the current research only focuses on a segment of the drop impact process in electric fields, lacking a comprehensive physical picture of the impact dynamics. In this work, we carried out a detailed experimental and numerical investigation covering the entire impact process that consists of the precontact stage (drop deformation when falling through the electric field), initial contact stage (evolving of air lubrication film and bubble entrapment), and postcontact stage (spreading, retraction, splashing, or jetting).

The paper is organized as the following. The experimental setup and numerical model are presented in Sec. II. In Sec. III A, we discuss the electrohydrodynamic behavior of the drop. Specifically, the dynamics of the drop impacting in electric fields consists of three stages: Stage I, the stretching deformation of the drop after being exposed in the electric field (Sec. III B); Stage II, the initial contact of the drop with the substrate and the evolving of the bottom air film (Sec. III C); and Stage III, the spreading, receding, jetting, and fragmentation (Sec. III D) in strong electric fields. A phase diagram of the deposition state of a drop in an electric field is given to summarize the various postcontact phenomena (Sec. III E). Finally, we conclude our work in Sec. IV.
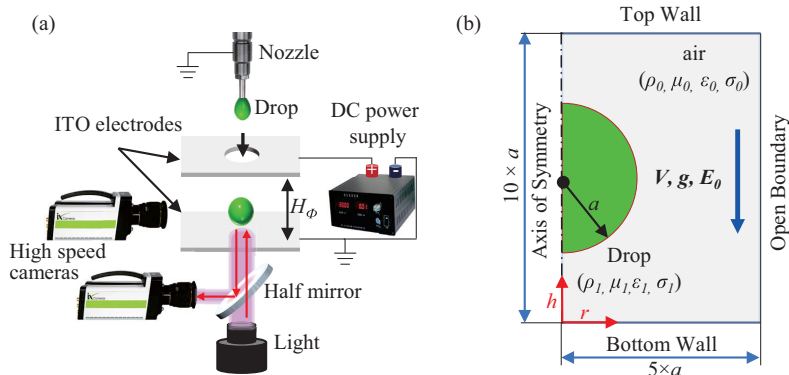
FIG. 1. (a) Schematic of the experimental setup. (b) Illustration of the computational domain of a leaky dielectric drop in an electric field.

II. EXPERIMENTAL SETUP AND NUMERICAL MODEL

A. Experimental setup

Figure 1(a) shows the experimental setup. An electric field is established between the top electrode and bottom electrode. Both electrodes are glass sides ($75 \times 25 \times 0.7$ mm^3) coated with 125-nm-thick indium tin oxide (ITO) to provide both good electric conductivity and optical transparency for imaging from the bottom. The electric field E_0 is the ratio of voltage difference Φ over the spacing H_Φ between the electrodes ($E_0 = \Phi/H_\Phi$). A hole of 3.5 mm in diameter is laser drilled on the top electrode for the drop injected from the nozzle entering the electric field. A polymethyl methacrylate film of 500 nm thickness is spin coated on the ITO to prevent charging the drop when contacting with the substrate. Afterwards, the substrate is modified with octadecyltrichlorosilane to achieve a $90°$ contact angle for water. A high-speed video camera (i-SPEED 726, iX Cameras) with a frame rate up to $272\,251$ fps is used for the bottom view to capture the fast initial contact. The resolving power is up to 1.35 μm/px and the exposure time is as short as 289 ns. The impacting behaviors from the side view are recorded with an i-SPEED 220 camera.

The drop is generated by pushing the deionized water through a stainless steel capillary with an outer diameter of 160 μm, and the radius of the drop is $a = 1.25 \pm 0.01$ mm. The impact velocity varies between 0.5 and 2.0 m/s as the release height (H) of the drop ranges from 7.5 to 200 mm. The Weber number is the dimensionless number that compares the ratio of kinetic energy to surface energy. In this study, the velocity in the Weber number is the instantaneous centroid velocity, which is not affected by the electric field and can be calculated by the release height of initial free fall ($\mathrm{We} = 4ag\rho_1 H/\gamma$, ranging from 5 to 135). The detailed material properties are shown in Table I.

TABLE I. Properties of the air and drop used in the experiments and numerical simulations. All the experiments are carried out at ambient pressure with room temperature. Here a is the radius of the drop, ρ is the liquid density, μ is the dynamic viscosity, σ is electrical conductivity, ε_r is the relative permittivity, and $\varepsilon_0 = 8.85 \times 10^{-12}$ is the dielectric constant of vacuum.

Liquid	a (mm)	ρ (kg/m^3)	μ (Pa s)	σ (S/m)	ε_r	γ (mN/m)
Drop	1.25 ± 0.01	998	1×10^{-3}	5.5×10^{-6}	80.18	72.7
Air		1.205	1.79×10^{-5}	1×10^{-50}	1.00	

B. Numerical model

In this work, a two-dimensional axisymmetric numerical domain is used for modeling the drop impact process in an electric field [Fig. 1(b)], of which the dimension is $5a \times 10a$. The numerical model combines the finite-volume method and a leaky dielectric model (LDM). The LDM assumes that the electrical charges are only distributed on the liquid-air interface because the charge relaxation time ($t_E = \varepsilon/\sigma$) is much shorter than the viscous time of fluid motion ($t_\mu = \rho a^2/\mu$) [49,50]. The volume of fluid method is implemented for capturing the liquid-air drop interface with the volume fraction α in a computational cell varying between [0, 1], where 0 and 1 represent air and liquid, respectively. The liquid-air interface is described by a thin layer of discrete basic computational volumes [51]. The governing equations of the drop motions are as follows:

$$\nabla \cdot \boldsymbol{U} = 0, \tag{1}$$

$$\frac{\partial(\rho \boldsymbol{U})}{\partial t} + \nabla \cdot (\rho \boldsymbol{U}\boldsymbol{U}) = -\nabla p + \nabla \cdot (\mu[\nabla \boldsymbol{U} + \nabla \boldsymbol{U}^T]) + \rho \boldsymbol{g} + \boldsymbol{f}_{\text{st}} + \boldsymbol{f}_e, \tag{2}$$

$$\boldsymbol{f}_{\text{st}} = \gamma \kappa (\nabla \alpha), \quad \kappa = \nabla \cdot \left(\frac{\nabla \alpha}{|\nabla \alpha|} \right), \tag{3}$$

where $\boldsymbol{f}_{\text{st}}$ is the surface tension stresses acting at the liquid-air interface and κ is the local curvature of the interface, which are obtained according to the continuous-surface-force model. $\boldsymbol{f}_e$ is the electric stress at the liquid-air interface given by

$$\boldsymbol{f}_e = \rho_e \boldsymbol{E} - \frac{1}{2}\boldsymbol{E}^2 \nabla \varepsilon, \tag{4}$$

where ($\boldsymbol{E}$) is the electric field,

$$\nabla \times \boldsymbol{E} = 0, \quad \boldsymbol{E} = -\nabla \Phi, \tag{5}$$

and the charge density (ρ_e) can be solved by the Gauss's theorem,

$$\rho_e = \nabla \cdot (\varepsilon \boldsymbol{E}) = -\nabla \cdot (\varepsilon \nabla \Phi). \tag{6}$$

Here the framework of OpenFOAM is chosen to implement the current numerical model [52–54]. An adaptive time step is used here to improve the computational efficiency with the minimum time step of 10^{-7} s. To ensure numerical continuity and stability, the Courant number, which represents the relative relationship between the time step and grid size, is set <0.5. For the bottom thin air film regime, the grid is further refined into 0.2 μm. Convergence of the solution is confirmed by checking the grid independence of the calculation results. It should be noted that the contact angle changes dynamically with the speed of the free surface advancing or receding in reality [55]. To focus on the effect of the electric field, a static contact angle of 90° (also consistent with experimental conditions) is used for this work.

III. RESULTS AND DISCUSSIONS

A. Electrohydrodynamics of drop impacting under electric fields

Figure 2 shows a few impact sequences from experiment and simulation in different electric field strengths. Here a dimensionless parameter of the electric field intensity (Γ_E) is defined to quantify the intensity of the electric field ($\boldsymbol{E}_0$):

$$\Gamma_E = \boldsymbol{E}_0 / \boldsymbol{E}_T, \tag{7}$$

where $\boldsymbol{E}_T$ is the maximum electric field strength proposed by Taylor [56], beyond which the drop disintegrates. $\boldsymbol{E}_T$ is expressed as:

$$\boldsymbol{E}_T = \frac{c}{2(\pi)^{1/2}} \left(\frac{\gamma}{\varepsilon_0 a} \right)^{1/2}. \tag{8}$$
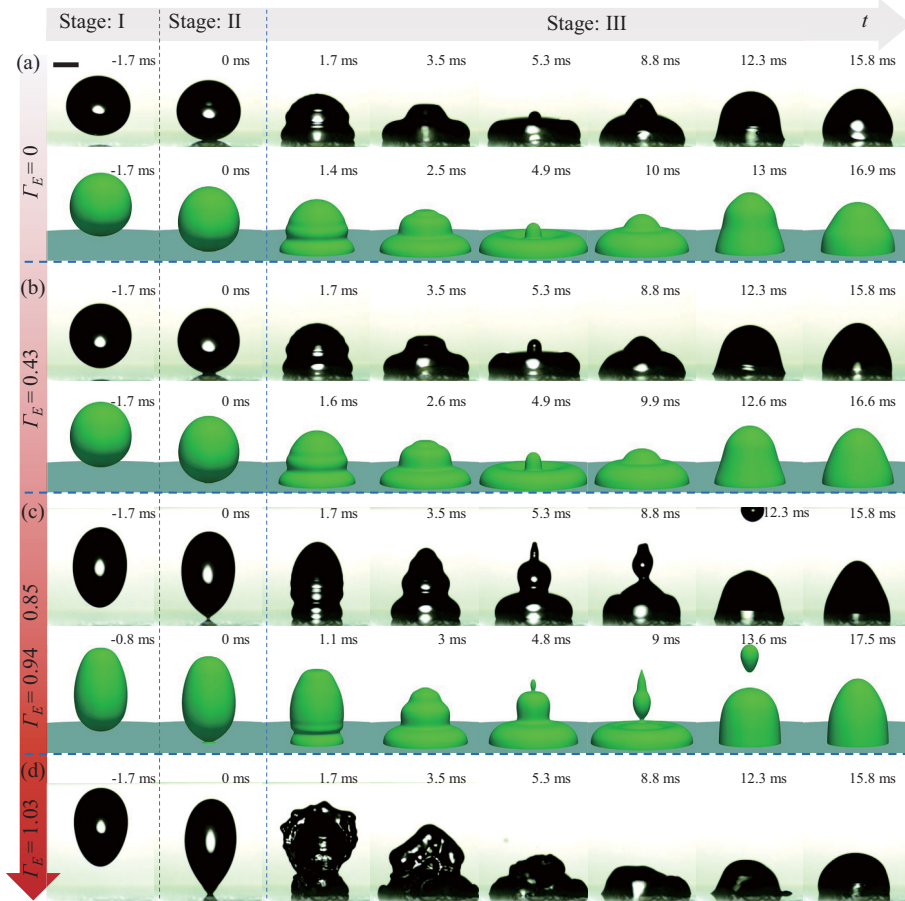
FIG. 2. The impact sequences from experiment and simulation in different electric field strengths (Γ_E). The spreading and receding process with $\Gamma_E = 0$ (a), $\Gamma_E = 0.43$ (b), $\Gamma_E = 0.85$, and $\Gamma_E = 0.94$ (c). The disintegration of the drop with $\Gamma_E = 1.03$ (d). The drop impacts the substrate at We = 5.1. The experimental images and simulation images show a good agreement when $\Gamma_E < 1$. Scale bar: 1 mm.

For water in the air, Basaran showed that $c = 1.625$ by fitting the experimental parameters [57]. Therefore, $\boldsymbol{E}_T = 1.176$ KV/mm in this study.

Unless otherwise specified, the moment of the contact of the drop on the substrate is marked as the initial contact time $t = 0$ ms. The uncertainty of the initial contact time is half of the imaging time interval ($\sim$0.06 ms) in the experiment. Figure 2(a) shows that the capillary waves are excited and propagate along the drop surface, which makes the spherical drop deforms into a pyramidal shape after contacting with the surface without electric field, as in Ref. [58]. The wavelength of the capillary wave λ scales with $\gamma/(\rho U)^2$. When a weak electric field is applied ($\Gamma_E = 0.43$), the spreading and receding seem to be approximately the same as that without electric field, except that the sessile drop exhibits a cone shape [Fig. 2(b)]. With stronger electric field ($\Gamma_E = 0.85$), the electrohydrodynamic behavior changes dramatically [Fig. 2(c)]: Initially, the drop deforms from spherical to ellipsoidal, forming a sharp central point contact with the substrate [Fig. 2(c), 0 ms]. The surface capillary wave has similar wavelength but noticeably greater amplitude than that of the neutral drop impact. The increased capillary wave amplitude causes pinch-off at the top of the drop, generating a small daughter droplet from the apex, which is fundamentally different from the
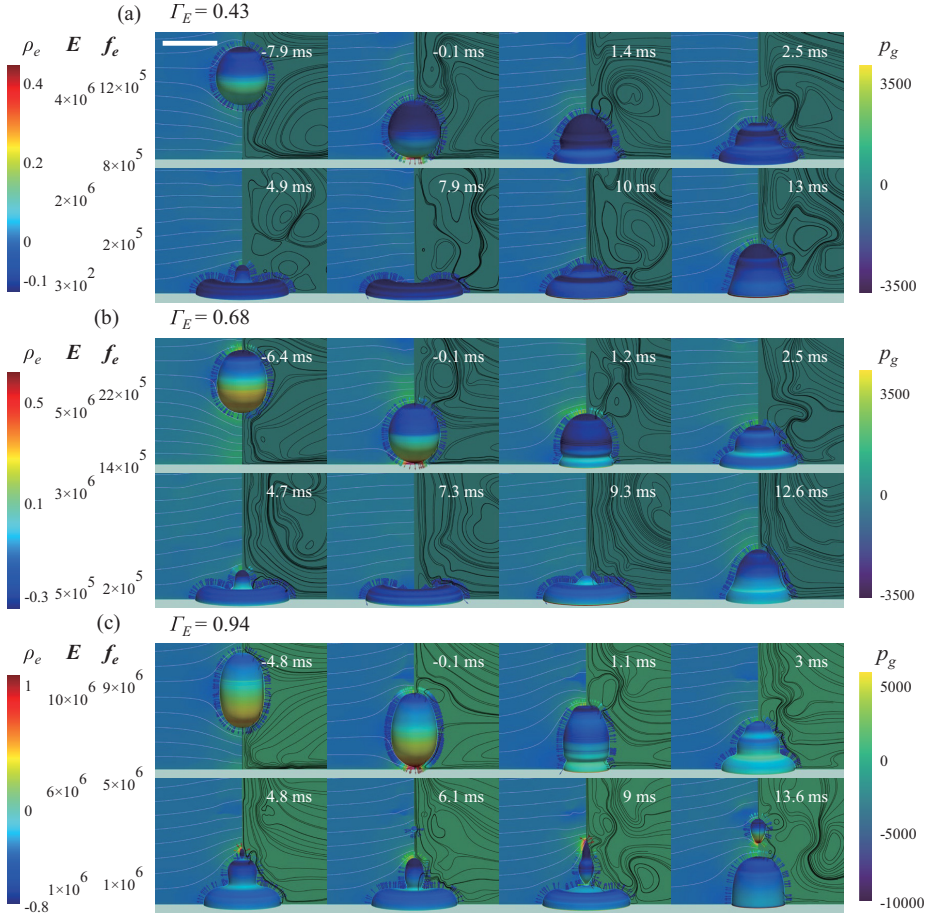
FIG. 3. The electric field and flow field with different Γ_E. Each unit figure consists of three parts: a superposition of the electric field strength $\boldsymbol{E}$ and electric isopotentials Φ (left half); a superposition of the polarization charge density ρ_e and vector of electric stresses $\boldsymbol{f}_e$ (at the drop interface); a superposition of the streamline of the velocity $\boldsymbol{U}$ and the gauge pressure p_g (right half). (a) $\Gamma_E = 0.43$, (b) $\Gamma_E = 0.68$, (c) $\Gamma_E = 0.94$. The drop impacts the substrate at We = 5.1. Scale bar: 2.5 mm.

singular jetting phenomena due to the collapse of the air cavity [58]. Under the stronger electric field, the top of the sessile drop is sharper. When the electric field is further increased beyond the Taylor limit of the critical field ($\Gamma_E = 1.03$), the top half of the drop is subject to strong electric stress, and the impact triggered capillary wave quickly destabilizes the surface and disintegrate the drop [Fig. 2(d), 1.7 ms].

To better understand the mechanism of the electrical field during the drop impact, the electric field and flow field with different Γ_E is shown in Fig. 3. Each unit figure consists of three parts: a superposition of the electric field strength $\boldsymbol{E}$ and electric isopotentials Φ (left half), and a superposition of the polarization charge density ρ_e and vector of electric stresses $\boldsymbol{f}_e$ (at the drop interface), and a superposition of the streamline of the velocity $\boldsymbol{U}$ and the gauge pressure p_g (right half). Typically, when the drop enters the domain with vertical electric field, the drop is polarized with equal positive and negative charge are distributed on the lower and upper ends of the drop, respectively. The amount of positive or negative charges ($Q = -3\pi\varepsilon_0 a^2 \boldsymbol{E}_0$) can be obtained by Taylor's analytical solution of a spherical drop suspended in an electric field [59]. The electrical

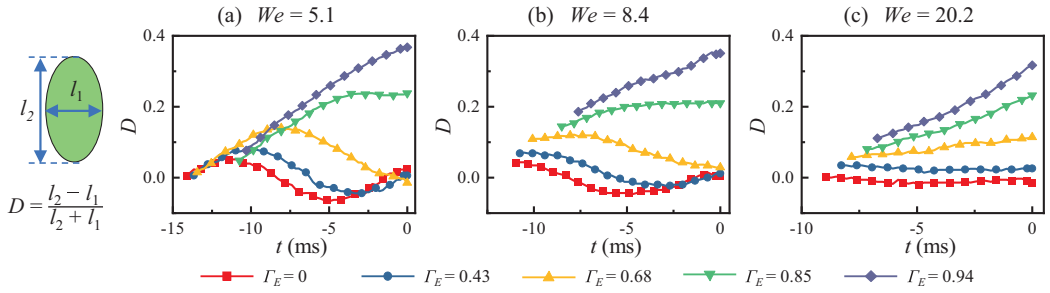FIG. 4. The variation in D after entering the electric field varies with different Γ_E. (a) We = 5.1. (b) We = 8.4. (c) We = 20.2. The moment of contacting as the reference time $t = 0$ ms.

field ($\boldsymbol{E}$) near the drop surface is modified by the polarized charges, resulting in the surface electric stresses ($\boldsymbol{f}_e$) field. $\boldsymbol{f}_e$ deforms the drop and redistributes the polarized charge, which in turn affects its own distribution. Similarly, both the surface electric stresses and the drop deformation are directly affected by the external electric field intensity (see the first two pictures of each impact sequence in Fig. 3).

Before the contact, as the drop approaches the substrate (the distance $\delta \to 0$), the polarized charges induced at the bottom quickly concentrate in a small area, and $\boldsymbol{E}$ at the bottom of the drop increases rapidly (see $t = -0.1$ ms). Using the mirror charge model of the dipole, the electric field at the drop bottom is $\boldsymbol{E}_B \sim a\boldsymbol{E}_0/\delta$ [47]. Therefore, the radius of drop bottom curvature decreases with higher Γ_E, resulting in a central point contact of the drop on the substrate. As the drop wets the substrate, the largest positive curvature of drop surface shifts from the drop bottom to the crests of capillary waves gradually, which redistributes the surface electric stresses ($\boldsymbol{f}_e$). The instantaneous change in $\boldsymbol{f}_e$ is the main reason for the different electrohydrodynamic behavior of spreading and receding compared with the impact without electric fields. When $\Gamma_E = 0.94$, a satellite droplet is ejected from the drop apex because of the convergence of capillary waves. As the sessile drop enters equilibrium state, the upper surface of the drop is still effected by the upward electric stresses, which deforms the drop from a hemispherical crown to a cone shape. The curvature of the cone increases with higher Γ_E.

Therefore, the difference in electrohydrodynamic behavior during the drop impact in the vertical electric field includes (1) the drop stretches when it enters an electric field, (2) the bottom of the drop forms a sharp cone when contacting with the substrate, and (3) jetting may occur after the impact. In the next section we discuss the EHD behavior in details.

B. Stage I: Drop deformation prior to contact

The drop undergoes an ellipsoidal deformation accompanied with weak oscillations caused by electric stresses when falling through the electric field. The degree of the drop deformation is quantified by the parameter D [60]:

$$D = (l_2 - l_1)/(l_2 + l_1), \tag{9}$$

where l_1 and l_2 are the lengths of the vertical and parallel axis of the deformed drop relative to the electric field, respectively (Fig. 4). Figure 4 shows that the variation in D after entering the electric field varies with different Γ_E and We. The lengths of l_1 and l_2 are extracted from high-speed images using a MATLAB program. The moment a drop completely enters the camera view is marked as the time reference $t = 0$ ms. The falling time before contact depends on the impact velocity of the drop with the same camera imaging parameters. When $\Gamma_E = 0$, there is a slight sinusoidal oscillation of the drop ($D_{\max} \approx 0.05$) in different We caused by the initial pinch-off from the capillary. The oscillation is damped by viscosity at higher We, simply because of the shorter falling time. As

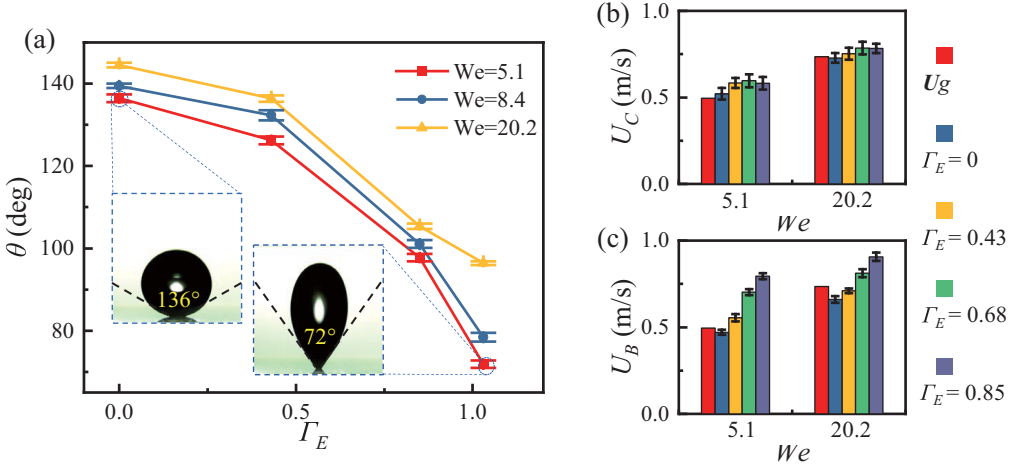FIG. 5. The shape of the drop at the moment of initial contact with different Γ_E and We. (a) The bottom cone angle (θ). As the Γ_E increases, the θ decreases quickly. The instantaneous centroid velocity U_C (b) and the bottom velocity of the drop U_B (c) when the drop contacts the substrate with different Γ_E.

shown in Figs. 4(a) and 4(b), with a small impact velocity (We = 5.1 and We = 8.4), the amplitude of the drop oscillation is increased ($D_{\max} \approx 0.14$) in the vertical electrical field ($\Gamma_E = 0.43$ and $\Gamma_E = 0.68$). With stronger electrical fields ($\Gamma_E = 0.85$ and $\Gamma_E = 0.94$), the initial stretching deformation increases, and the drop oscillation transforms into vertical axial stretching ($D_{\max} \approx 0.37$). With a higher impact velocity [We = 20.2, Fig. 4(c)], there is only stretching deformation with no significant oscillatory deformation, and D increases with higher Γ_E.

Figure 5(a) shows the shape of the drop at the moment of initial contact, whose time uncertainty is about 0.06 ms. With lower We and higher Γ_E, the stretching deformation is more profound, making a sharper drop bottom. The sharper tip is attributed to two factors: First, it is easier to form a conical tip with lower We because there is more time for a slower descending drop to respond to the electric field and deform; second, a higher air film pressure is built up with a larger velocity, which counters the EHD deformation. For example, the drop impact with We = 5.1, as Γ_E increases, the bottom cone angle decreases from 136.5° at $\Gamma_E = 0$ to 71.8° at $\Gamma_E = 1.03$. This can be explained as follows: First, there is less time for a fast descending drop to respond to the electric field and deform; second, a higher pressure of the air film is generated with a larger velocity for the drop, which counteracts the deformation caused by the electric field.

The velocity of the drop bottom prior to contact consists of two parts: (i) the free-fall velocity under the action of gravity and (ii) the bottom stretching deformation velocity. We show the instantaneous centroid velocity $\boldsymbol{U}_C$ of the drop and the instantaneous velocity $\boldsymbol{U}_B$ of the drop bottom after entering the electric field varying with different Γ_E in Figs. 5(b) and 5(c), respectively. The data suggests that U_C increases slightly with Γ_E, while the bottom velocity U_B increases noticeably with Γ_E, which is due to the bottom stretching deformation.

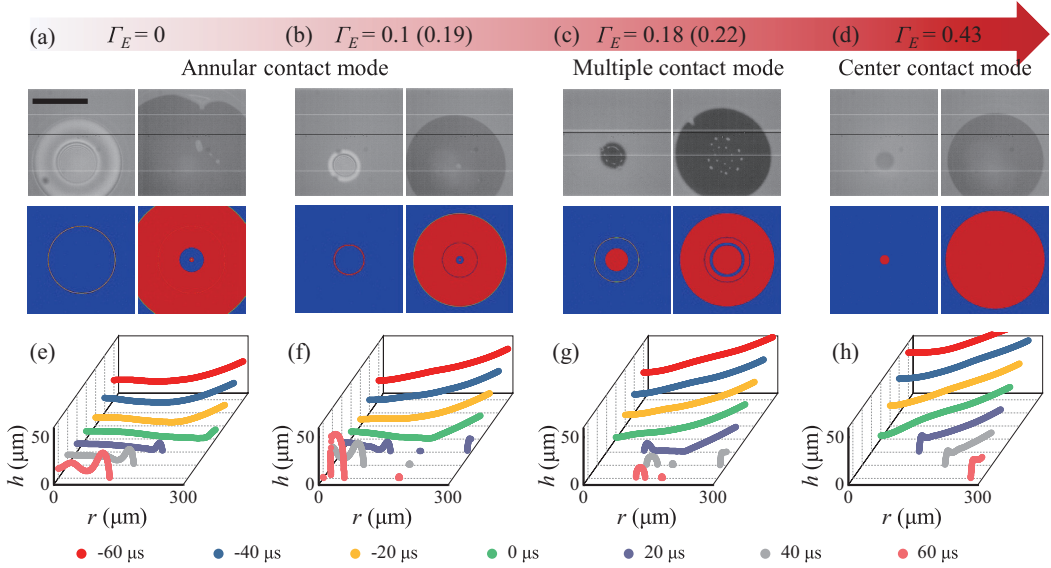## C. Stage II: Initial contact with the substrate

Figures 6(a)–6(d) shows the interference fringes of the air film captured from the bottom-view camera and the substrate wetting map obtained numerically at different Γ_E of three typical contact modes. Experimentally, the initial contact is identified by the appearance of dark spots, which are caused by the reduced light reflection after the drop wets the ITO substrate. The temporal uncertainty is about 6.7 μs. Hicks *et al.* gave the theoretical prediction of the initial contact radius (L_0) of the

FIG. 6. The interference fringes of the air film captured from the bottom-view camera and the substrate wetting map obtained numerically at different Γ_E of three typical contact modes. Annular contact mode: (a) a normal size Newton's ring retracting into an air bubble with $\Gamma_E = 0$; (b) a smaller Newton's ring retracting into a smaller air bubble with $\Gamma_E = 0.1$ and $\Gamma_E = 0.19$. Multiple contact mode: (c) Multiple concentric circular contact lines with toroid air bubbles entrapped underneath with $\Gamma_E = 0.18$ and $\Gamma_E = 0.22$. Center contact mode: (d) A single dark circular disk without Newton's ring and air bubble with $\Gamma_E = 0.43$. [(e)–(h)] The profiles of the bottom air film ($h \sim r$) evolving with time for above contact modes. Here drop impacts the substrate at We = 8.4. Scale bar: 300 μm. The time interval is 20 μs in simulations.

drop deposited on the substrate based on an incompressible model [61]:

$$L_0 = 3.8 \left(\frac{4\mu_0}{\rho_1 U} \right)^{1/3} a_B^{2/3}, \tag{10}$$

where a_B is the local radius of curvature at the bottom of the drop. Here L_E is defined as the air film radius varying with time in the droplet impact under the electric field [see Fig. 7(a)], where L_{E0} is the initial contact radius.

With We = 8.4, the initial contact radius predicted by Eq. (10) is $L_E = 232$ μm. In our study, without the electrical field ($\Gamma_E = 0$), a ring contact firstly occurs, whose radius is 195 and 259 μm in experiment and simulation, respectively [Fig. 6(a)], both in decent agreement with Eq. (10). Figure 6(e) shows that the drop bottom begins to be deformed and decelerated by the thin air cushion underneath for $h = 20$ μm, where the highest pressure is located at the bottom center. Then the drop bottom deforms into a dimple with the air disk expanding further. Soon with the generation of capillary waves, the air film converges rapidly to the center before it is pinched off.

When a relatively weak vertical electrical field is applied ($\Gamma_E = 0.1, 0.19$), the initial contact radius L_{E0} are reduced to 89.5 and 180 μm in experiment and simulation, respectively [Fig. 6(b)]. The drop bottom is flatted by the thin air cushion underneath until $h = 10$ μm [Fig. 6(f)]. Then the drop bottom deforms into a smaller dimple. Meanwhile, the increasing electric strength accelerates the edge of the air disk and leads to a smaller contact radius. Then the inner circular contact line recedes and the air film converges rapidly to the center into a smaller bubble subsequently. Figures 6(c) and 6(g) shows that with stronger electric field ($\Gamma_E = 0.18, 0.22$), the polarized charges accumulate at the lowest surface of the bottom, which deforms the drop bottom surface into a
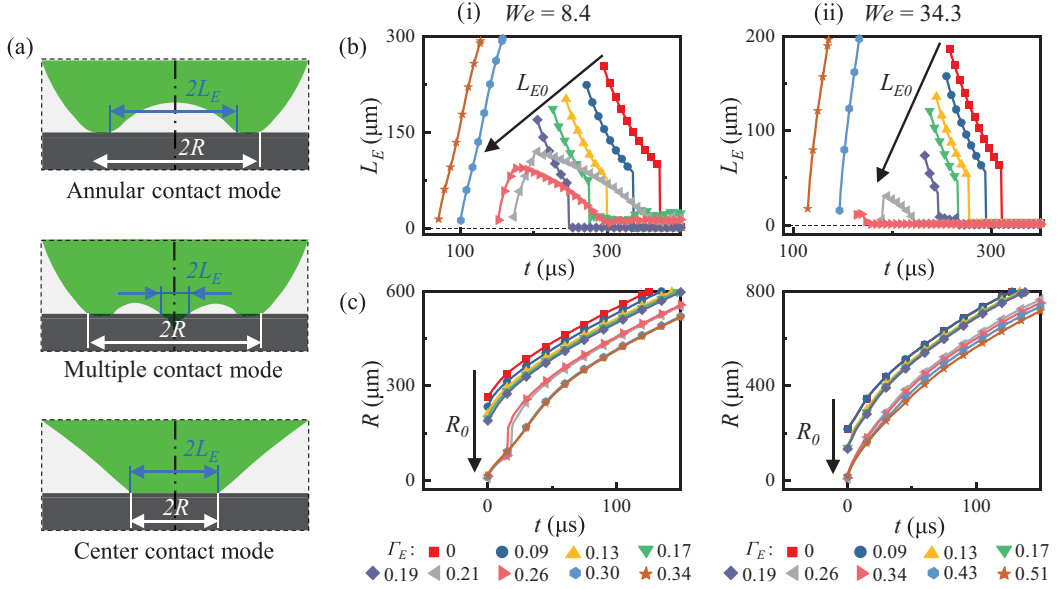
FIG. 7. (a) Schematic of the drop initial wetting on the substrate in three contact modes. The sequential evolution of air film radius L_E (b) and drop spreading radius R (c) with time for different electric field strengths with different impact velocities in simulations. L_{E0} and R_0 both decrease as the Γ_E increase.

wimple shape around the center. This results in multiple concentric circular contact lines with toroid air bubbles entrapped underneath. When the electrical field is further strengthened ($\Gamma_E = 0.43$), the bottom of the drop sharpens up before $h = 20\ \mu$m [Figs. 6(e) and 6(f)]. The lowest point of the drop bottom surface is accelerated and forms a cone tip to touchdown, resulting in a single dark circular disk. The wetting area expands from the central spot without any air bubble entrapment. For a thorough discussion of the air film structure at the initial contact, readers are referred to Ref. [47].

After the contact, the drop wets the substrate from the contact line to the center and outside, which is characterized by the air film radius L_E and the drop spreading radius R. Figure 7(b) shows the sequential evolution of the air film radius L_E with time for different Γ_E in simulations. When $\Gamma_E < 0.19$, the initial contact radius L_{E0} shrinks with the increase of Γ_E. Five lines of L_E under a weak electric field decrease from L_{E0} to zero, which represents that the air film converges to the center and forms a bubble. When $\Gamma_E = 0.21, 0.26$ and $\Gamma_E = 0.26, 0.34$ in We $= 8.4$ and We $= 34.3$, respectively, L_E first increases from zero to a peak value, and then gradually decreases to zero, which represents the multiple contact with concentric circular air rings. Further increasing Γ_E, L_{E0} shrinks to zero and L_E is equivalent to R in this case, showing an increasing trend all the time, which corresponds to that no air film is trapped in the subsequent wetting process. Figure 7(c) shows the drop spreading radius R history with different electric field strength from simulations. It is clear to see that the spreading radius R_0 with different We both reduce from L_{E0} to zero with the increase of Γ_E and every line of R increases until it reaches the maximum radius in the subsequent wetting process. All the above behavior changes can reflect that the electric field can adjust and eliminate the trapped bubbles.

D. Stage III: Spreading, jetting, and fragmentation

The postimpact electrohydrodynamic exhibit rich outcomes ranging from smooth spreading and receding to jetting. Unlike drop impact onto the superhydrophobic surface under the electric field
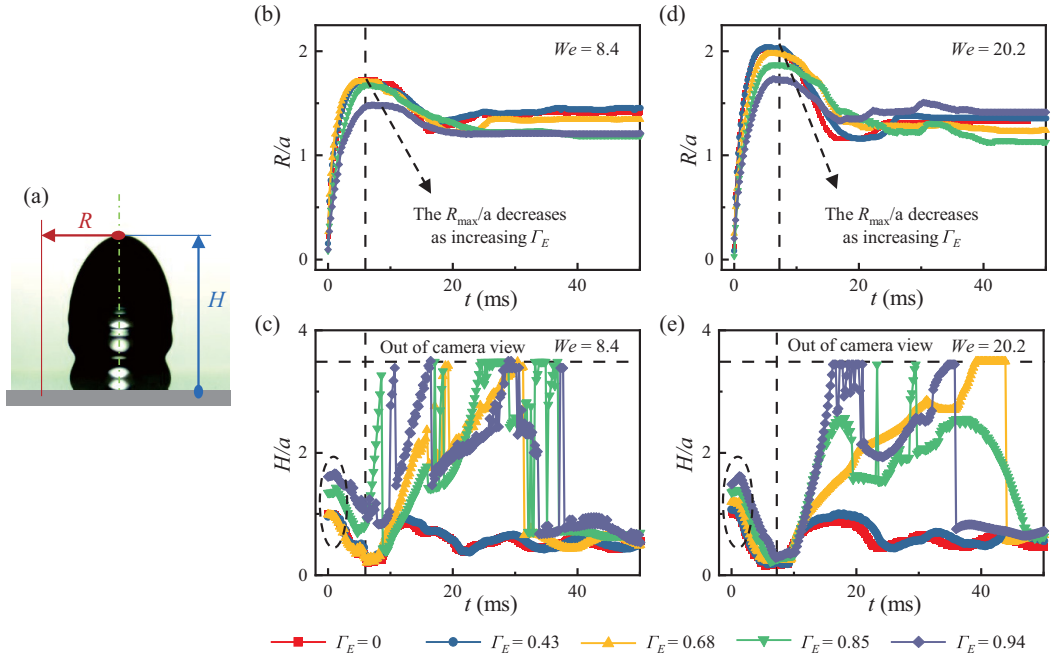
FIG. 8. (a) Schematic of the drop spreading on the substrate. The sequential evolution of the dimensionless spreading radius R/a [(b) and (d)] and free surface height H/a [(c) and (e)] with time for different electric field strengths with different impact velocities in experiments. The vertical and horizontal dotted lines in (b)–(e) are the time mark of the maximum R/a and the maximum height H/a with $\Gamma_E = 0$. The maximum R/a decreases with stronger Γ_E. The H/a shows a sharp falling when $\Gamma_E \geqslant 0.68$ because of the breakup of the sessile drop surface.

[48], no rebound behaviors are observed in this work. Here the dimensionless spreading radius R/a and the free surface height H/a are used to describe the postimpact electrohydrodynamics. Figure 8 shows the R/a and H/a obtained experimentally with different electric field strengths. The moment of initial contact between the drop and is marked as the time reference $t = 0$ ms. With no electrical field, Pasandideh-Fard *et al.* [62] derived the dimensionless maximum spread radius $R_{\max}/a$, which is obtained through a balance between the inertia and capillary forces with correction due to viscous dissipation and substrate wettability.

When the electrical field is applied, $R_{\max}/a$ decreases as Γ_E increases due to the upward electric stress pulling the top of the drop. The H/a continuously increases for a short time in the early spreading stage due to the electric stress pulling the top drop surface upward. When $R_{\max}/a$ is reached the height also decreases to the minimum H/a (Fig. 8). After $R_{\max}/a$ is reached, the drop starts to recoil due to surface tension, with the kinetic energy gradually being dissipated by the viscous effect. Finally, the contact line stops moving. Figures 8(c)–8(e) shows that when $\Gamma_E \leqslant 0.43$, H/a continues to oscillate after contact line receding. However, when $\Gamma_E \geqslant 0.68$, the surface of the sessile drop will break up, and the H/a shows an abrupt declining. Therefore, stronger Γ_E leads to earlier drop rupture and more daughter droplet ejections.

Based on the size of daughter droplets, three modes of drop top surface rupture can be classified. (i) A small droplet with diameter at least an order of magnitude smaller than the initial drop ejected at velocities 1.2 m/s from the apex of the drop during the spreading [Fig. 9(a)]. As the capillary wave propagates and converges to the top of the drop, the top will experience increasing electric stress because of the high local curvature. As shown in Fig. 10(a), the maximum electrical stress is located at the top of the drop, and the peak Laplace pressure is located at the first trough next
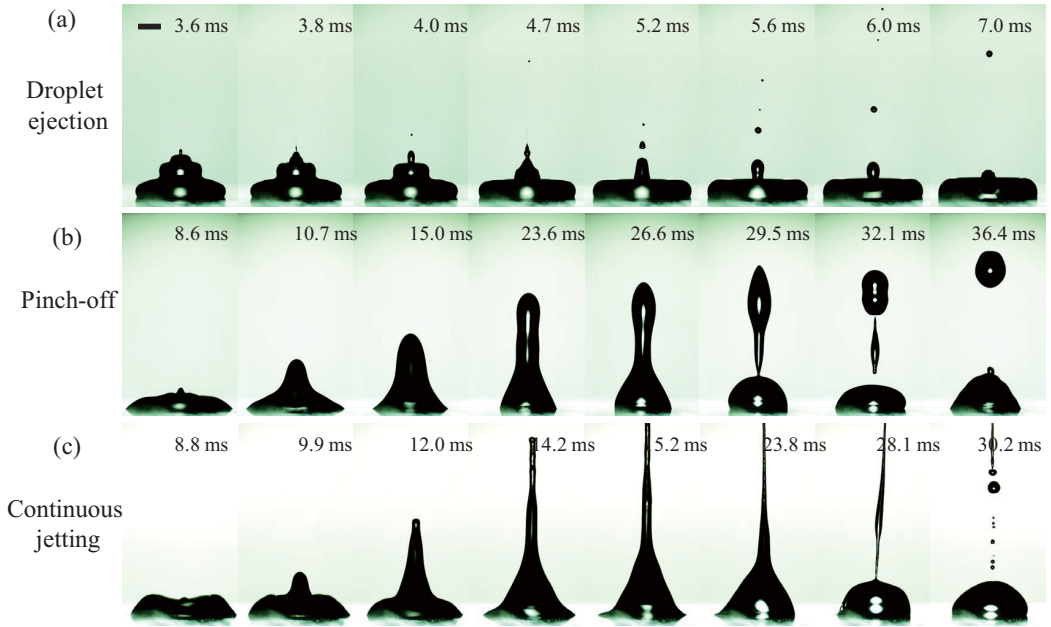
FIG. 9. Three modes of drop top surface rupture with different impact conditions. (a) A small droplet with diameter at least an order of magnitude smaller than the initial drop ejected during the spreading (We = 5.1, $\Gamma_E = 0.85$). (b) A large drop of few hundred micrometers in diameter produced by pinch-off of the stretched drop during the receding (We = 8.4, $\Gamma_E = 0.68$). (c) A continuous jetting during the receding (We = 8.4, $\Gamma_E = 0.94$). Scale bar: 1 mm.

to the top. In turn, the unevenly distributed electric stresses may perturbs the neck and triggers the Rayleigh-Plateau instability enhancing the pinching effect at the trough, which leads to the ejection of small satellite droplets. Then the ejected droplet flew upward due to the electric field. Next, a new neck forms and a similar ejection process may repeat several times. (ii) A large drop of few hundred micrometers in diameter is produced by pinch-off of the stretched drop [Fig. 9(b)]. A jet tip is formed at the top surface due to the receding inertia and the upward electric stress [Fig. 10(b)]. The larger We number also causes stronger recoiling and longer jet, which breaks up in the middle with a velocity of ∼0.3 m/s under the action of surface tension within a timescale of $\tau = \sqrt{\rho R_j^3 / \gamma}$ ($\tau \approx 116$ μs for the jet with the initial jet radius $R_j \approx 97$ μm) [63]. Note that the jet instability may produce two or three small drops here, which may remerge with the mother drop or fly to the top electrode. (iii) A continuous jetting [Fig. 9(c)]. When the electric field strength is further increased ($\Gamma_E = 0.94$), the stretching effect of the electric stress, in addition to the receding inertia, becomes more obvious [Fig. 10(c)]. The jet rises at velocities 0.64 m/s for nearly 20 ms, resulting in a nearly continuous jet. As a large portion of liquid is ejected, the polarized charge on the drop surface decreases rapidly. The jet then breaks up into multiple small droplets. Eventually, the residual liquid on the substrate forms a smaller sessile drop.

When the electric field reaches a critical value, the drop may become unstable and disintegrate [64,65]. Figure 11 shows four types of drop disintegration observed in this study. All disintegration appears at the location of the highest curvature of the drop, which also have the highest local field strength. Once the disintegration occurs, the cohesive failure of the drop results in crown formation and the expansion of the liquid sheet [66,67]. The images suggest that the electric discharge will dominate over the effect of surface tension and form a crown shape with a higher surface-to-volume ratio and irregular shape. The liquid film quickly collapses or shrinks.
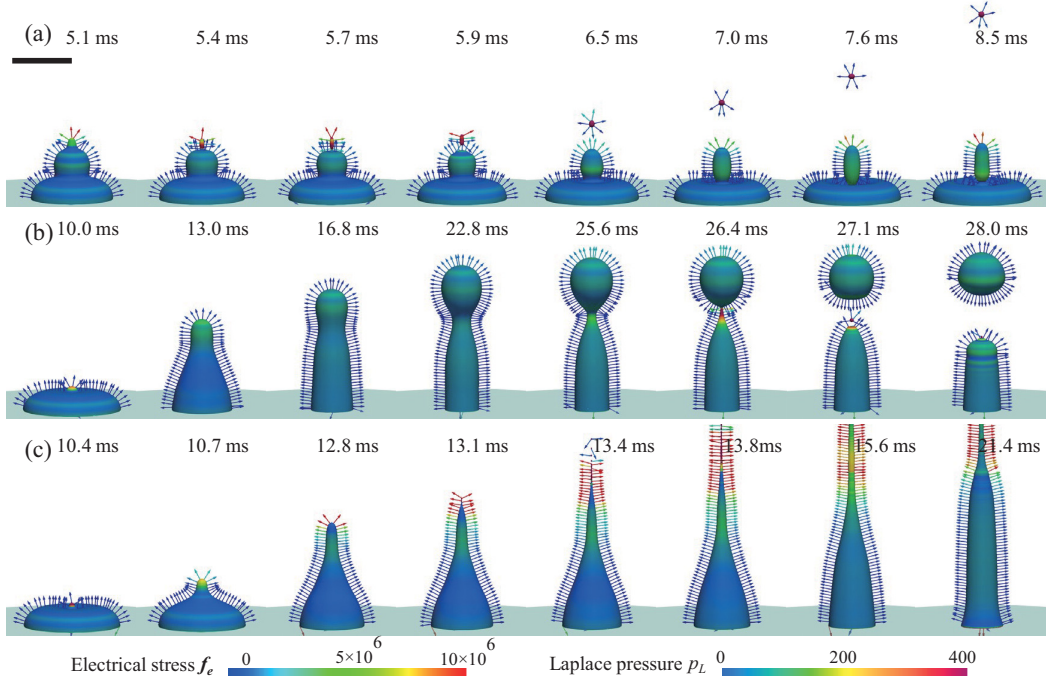
FIG. 10. The corresponding three modes of drop top surface rupture in simulations. (a) A small droplet with diameter at least an order of magnitude smaller than the initial drop ejected during the spreading (We = 5.1, $\Gamma_E = 0.94$). (b) A large drop of few hundred micrometers in diameter produced by pinch-off of the stretched drop during the receding (We = 8.4, $\Gamma_E = 0.68$). (c) A continuous jetting during the receding (We = 8.4, $\Gamma_E = 0.94$). Scale bar: 2.5 mm.

E. Phase diagram of impact modes

We summarize our experimental and numerical results in Fig. 12, which includes four drop deposition states that separate the whole phase diagram into three areas. In the lower right region, i.e., larger We and smaller Γ_E, the external electric field is not sufficiently strong to reduce the initial contact radius of the drop L_{0E} to 0, corresponding to the state of drop deposition with air bubble entrapment at the bottom. The middle region in the phase diagram (with more moderate Γ_E) corresponds to the stable deposition of drops without bubble capture at the bottom. In this region, the external electric field reduces the initial contact radius of the droplet to 0, but the associated electric stress is not strong enough to pull the drop top surface up. The upper left region in the phase diagram (larger Γ_E) also has point contact, but the stronger electric field stretches the drop surface to form jetting or even disintegration in the recoiling process. This phase diagram suggests that choosing the appropriate amplitude of external electric field strength and We number can properly regulate the drop impact process to avoid air bubble entrapment as well as drop surface fragmentation, thus achieving the desired high-quality drop deposition. In practical applications, we note that the droplets produced by inkjet are one to two orders of magnitude smaller than the drop studied in this work. The droplet radius (a) affects both the electric stress f_{eB} and the lubrication pressure p_g, but with different scaling: $f_{eB} \sim \frac{\varepsilon_0}{\delta^2} a^2 \boldsymbol{E}_0^2$ and $p_g \sim \frac{\mu_0}{\delta^2} a \boldsymbol{U}$ [47]. To achieve deposition without bubbles at the same impact speed, the electric stress must be at least comparable with the lubrication pressure, i.e., $f_{eB} \sim p_g$, or $\boldsymbol{E}_0 \sim a^{-1/2}$. Hence the applied electric field strength is expected to increase as the drop radius shrinks for bubble-free deposition.
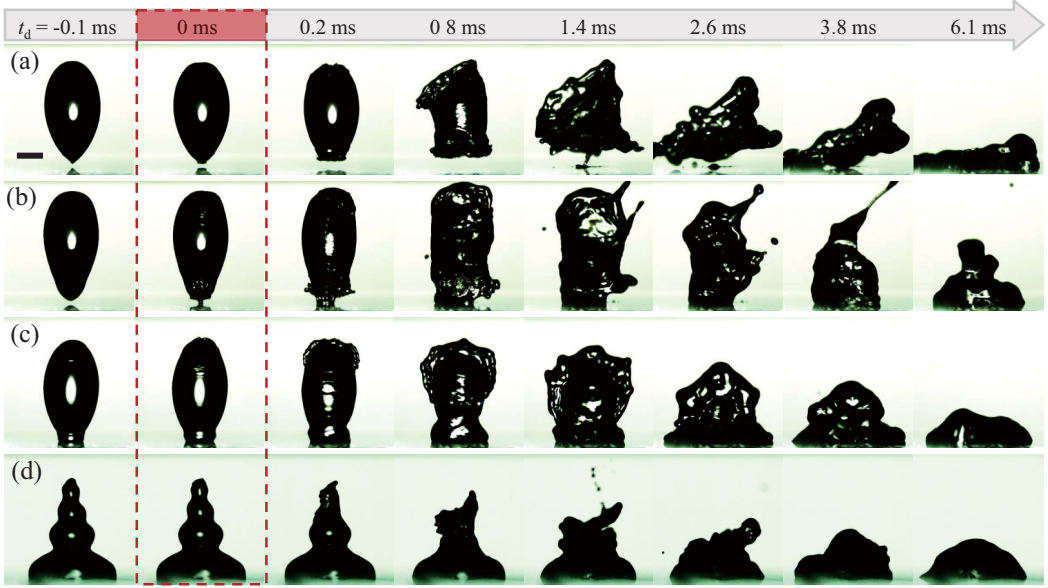
FIG. 11. Four types of drop disintegration. (a) bottom disintegration in the precontact stage (We = 5.1, Γ_E = 1.03); (b) bottom disintegration in the initial contact state (We = 5.1, Γ_E = 1.28); (c) top disintegration in the initial contact state (We = 5.1, Γ_E = 1.28); (d) top disintegration during spreading in the postcontact stage (We = 8.4, Γ_E = 1.03). The moment of drop disintegration that occurs is marked as reference time t_d = 0 ms in this picture. Scale bar: 1 mm.

IV. CONCLUSIONS

In summary, the electrohydrodynamic of a drop impacting onto a solid surface under an external electric field is investigated experimentally and numerically, covering the overall impact process that consists of the precontact stage (drop deformation when falling through the electric field), initial contact stage (evolving of air lubrication film and air bubble entrapment), and postcontact stage (spreading, retraction, splashing or jetting, and fragmentation). The results show that the presence of electric field changes the drop impact behaviors because of the separated polarized charge and
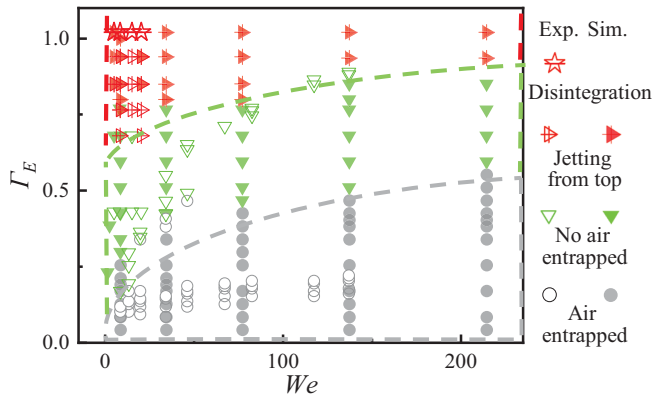

FIG. 12. Phase diagram for drop deposition modes with different Γ_E and We in experiments and simulations. The solid patterns for numerical simulations and the hollow patterns for experiments.

the associated surface electric stress, which are induced by the electric field and augmented by the drop deformations.

In the precontact stage, under the stronger electric fields, the initial modest drop oscillation grows into a vertically stretched spindle and the impact velocity of the drop bottom is increased. As the drop approaches the substrate, the electric stress at the south pole increases rapidly, which sharpens the bottom surface into a conical shape. The cone angle is determined by both the impact velocity and the electric field strength. The initial contact radius L_{E0} can shrink to 0 as the Γ_E increases to a certain value, which is depended on the impact velocity. In the postcontact stage, the surface electric stress tends to pull the drop upward, which reduces the maximum spreading radius R/a and form a cone shape sessile drop instead of a hemispherical crown. With stronger Γ_E, the drop disintegrates and several jetting modes are formed, which are classified from the size of daughter droplets. Finally, the various drop deposition modes are summarized in a phase diagram, which sheds light on identifying appropriate electric fields for high-quality drop depositions without air bubble entrapments or jettings in drop deposition-based applications such as inkjet/electrohydrodynamic printing and spray coating. However, the droplet radius in the above printing technology ranges from the micron to the hundred-micron. The regulation of the electric field may be needed further research subsequently to satisfy the high-quality deposition in microdroplet.

[1] S. T. Thoroddsen, T. G. Etoh, and K. Takehara, High-speed imaging of drops and bubbles, Annu. Rev. Fluid Mech. **40**, 257 (2008).

[2] C. Josserand and S. T. Thoroddsen, Drop impact on a solid surface, Annu. Rev. Fluid Mech. **48**, 365 (2016).

[3] D. B. van Dam and C. L. Clerc, Experimental study of the impact of an ink-jet printed droplet on a solid substrate, Phys. Fluids **16**, 3403 (2004).

[4] M. J. Thoraval, K. Takehara, T. G. Etoh, and S. T. Thoroddsen, Drop impact entrapment of bubble rings, J. Fluid Mech. **724**, 234 (2013).

[5] H. Zhao, X. Han, J. Li, W. Li, T. Huang, P. Yu, and L. Wang, Numerical investigation of a droplet impacting obliquely on a horizontal solid surface, Phys. Rev. Fluids **7**, 013601 (2022).

[6] H. Wu, Y. Tian, H. Luo, H. Zhu, Y. Duan, and Y. Huang, Fabrication techniques for curved electronics on arbitrary surfaces, Adv. Mater. Technol. **5**, 2000093 (2020).

[7] Y. Huang, H. Wu, L. Xiao, Y. Duan, H. Zhu, J. Bian, D. Ye, and Z. Yin, Assembly and applications of 3d conformal electronics on curvilinear surfaces, Mater. Horiz. **6**, 642 (2019).

[8] D. Ye, Y. Ding, Y. Duan, J. Su, Z. Yin, and Y. A. Huang, Large-scale direct-writing of aligned nanofibers for flexible electronics, Small **14**, e1703521 (2018).

[9] Y. Li, K. Chang, J. Chang, B. Yu, L. Liu, B. Liu, X. Zhao, and W. Deng, Printed kirigami organic photovoltaics for efficient solar tracking, Adv. Funct. Mater., **32**, 2204004 (2022).

[10] M. Zhu, Y. Duan, N. Liu, H. Li, J. Li, P. Du, Z. Tan, G. Niu, L. Gao, Y. Huang, Z. Yin, and J. Tang, Electrohydrodynamically printed high-resolution full-color hybrid perovskites, Adv. Funct. Mater. **29**, 1903294 (2019).

[11] B. Derby, Inkjet printing of functional and structural materials: Fluid property requirements, feature stability, and resolution, Annu. Rev. Mater. Res. **40**, 395 (2010).

[12] S. C. Ligon, R. Liska, J. Stampfl, M. Gurr, and R. Mulhaupt, Polymers for 3d printing and customized additive manufacturing, Chem. Rev. **117**, 10212 (2017).

[13] H. Yi, L. h. Qi, J. Luo, Y. Jiang, and W. Deng, Pinhole formation from liquid metal microdroplets impact on solid surfaces, Appl. Phys. Lett. **108**, 041601 (2016).

[14] C. Antonini, J. B. Lee, T. Maitra, S. Irvine, D. Derome, M. K. Tiwari, J. Carmeliet, and D. Poulikakos, Unraveling wetting transition through surface textures with x-rays: Liquid meniscus penetration phenomena, Sci. Rep. **4**, 1 (2014).

[15] Y. Liu, P. Tan, and L. Xu, Kelvin-helmholtz instability in an ultrathin air film causes drop splashing on smooth surfaces, Proc. Natl. Acad. Sci. USA **112**, 3280 (2015).

[16] L. Zhang, T. Soori, A. Rokoni, A. Kaminski, and Y. Sun, Thin film instability driven dimple mode of air film failure during drop impact on smooth surfaces, Phys. Rev. Fluids **6**, 044002 (2021).

[17] P. D. Hicks and R. Purvis, Air cushioning and bubble entrapment in three-dimensional droplet impacts, J. Fluid Mech. **649**, 135 (2010).

[18] S. Mandre, M. Mani, and M. P. Brenner, Precursors to Splashing of Liquid Droplets on a Solid Surface, Phys. Rev. Lett. **102**, 134502 (2009).

[19] H. C. Qi, T. Y. Wang, and Z. Z. Che, Air layer during the impact of droplets on heated substrates, Phys. Rev. E **101**, 043114 (2020).

[20] W. Bouwhuis, R. C. A. van der Veen, T. Tran, D. L. Keij, K. G. Winkels, I. R. Peters, D. van der Meer, C. Sun, J. H. Snoeijer, and D. Lohse, Maximal Air Bubble Entrainment at Liquid-Drop Impact, Phys. Rev. Lett. **109**, 264501 (2012).

[21] E. Q. Li, I. U. Vakarelski, and S. T. Thoroddsen, Probing the nanoscale: The first contact of an impacting drop, J. Fluid Mech. **785**, R2 (2015).

[22] K. R. Langley, A. A. Castrejon-Pita, and S. T. Thoroddsen, Droplet impacts onto soft solids entrap more air, Soft Matter **16**, 5702 (2020).

[23] D. Shen, G. Zou, L. Liu, W. W. Duley, and Y. N. Zhou, Investigation of splashing phenomena during the impact of molten sub-micron gold droplets on solid surfaces, Soft Matter **12**, 295 (2016).

[24] S. T. Thoroddsen, T. G. Etoh, and K. Takehara, Air entrapment under an impacting drop, J. Fluid Mech. **478**, 125 (2003).

[25] E. Q. Li, K. R. Langley, Y. S. Tian, P. D. Hicks, and S. T. Thoroddsen, Double Contact During Drop Impact on a Solid Under Reduced Air Pressure, Phys. Rev. Lett. **119**, 214502 (2017).

[26] L. Xu, W. W. Zhang, and S. R. Nagel, Drop Splashing on a Dry Smooth Surface, Phys. Rev. Lett. **94**, 184505 (2005).

[27] Q. Vo and T. Tran, Mediation of lubricated air films using spatially periodic dielectrophoretic effect, Nat. Commun. **12**, 4289 (2021).

[28] T. Maitra, M. K. Tiwari, C. Antonini, P. Schoch, S. Jung, P. Eberle, and D. Poulikakos, On the nanoengineering of superhydrophobic and impalement resistant surface textures below the freezing temperature, Nano Lett. **14**, 172 (2014).

[29] S. R. Mahmoudi, G. S. P. Castle, and K. Adamiak, Retraction control of an impacted dielectric droplet through electrical pressure, Soft Matter **8**, 808 (2012).

[30] Q. Wang, Z. Suo, and X. Zhao, Bursting drops in solid dielectrics caused by high voltages, Nat. Commun. **3**, 1157 (2012).

[31] R. T. Collins, K. Sambath, M. T. Harris, and O. A. Basaran, Universal scaling laws for the disintegration of electrified drops, Proc. Natl. Acad. Sci. USA **110**, 4905 (2013).

[32] Q. M. Wang, M. M. Ma, and M. Siegel, Deformation and stability of a viscous electrolyte drop in a uniform electric field, Phys. Rev. Fluids **4**, 053702 (2019).

[33] W. Xu, J. Luo, J. Qin, and Y. Zhang, Maximum deformation of charged dielectric droplets, AIP Adv. **10**, 035013 (2020).

[34] J. Zhang, T.-Y. Han, J.-C. Yang, and M.-J. Ni, On the spreading of impacting drops under the influence of a vertical magnetic field, J. Fluid Mech. **809**, R3 (2016).

[35] Q. Liu, J. H. Y. Lo, Y. Li, Y. Liu, J. Zhao, and L. Xu, The role of drop shape in impact and splash, Nat. Commun. **12**, 3068 (2021).

[36] W. Deng and A. Gomez, The role of electric charge in microdroplets impacting on conducting surfaces, Phys. Fluids **22**, 051703 (2010).

[37] A. Shahriari, S. Das, V. Bahadur, and R. T. Bonnecaze, Analysis of the instability underlying electrostatic suppression of the leidenfrost state, Phys. Rev. Fluids **2**, 034001 (2017).

[38] F. Gao, H. Yi, L. Qi, R. Qiao, and W. Deng, Weakly charged droplets fundamentally change impact dynamics on flat surfaces, Soft Matter **15**, 5548 (2019).

[39] J. Zhang, J. D. Zahn, and H. Lin, Transient solution for droplet deformation under electric fields, Phys. Rev. E **87**, 043008 (2013).

[40] P. M. Vlahovska, Electrohydrodynamic instabilities of viscous drops, Phys. Rev. Fluids **1**, 060504 (2016).

[41] Q. Nie, Y. Huang, Z. Yin, and H. Fang, Large deformation of a conductive nanodroplet in a strong electric field, Phys. Fluids **32**, 022006 (2020).

[42] Y. N. Wang, D. L. Sun, Y. S. Li, S. Chen, and B. Yu, Migration behaviors of leaky dielectric droplets with electric and hydrodynamic forces, Phys. Rev. E **100**, 033113 (2019).

[43] R. Pillai, J. D. Berry, D. J. E. Harvie, and M. R. Davidson, Electrolytic drops in an electric field: A numerical study of drop deformation and breakup, Phys. Rev. E **92**, 013007 (2015).

[44] W. Yang, H. Duan, C. Li, and W. Deng, Crossover of Varicose and Whipping Instabilities in Electrified Microjets, Phys. Rev. Lett. **112**, 054501 (2014).

[45] P. M. Vlahovska, Electrohydrodynamics of drops and vesicles, Annu. Rev. Fluid Mech. **51**, 305 (2019).

[46] Z. Wang, Y. Tian, C. Zhang, Y. Wang, and W. Deng, Massively Multiplexed Electrohydrodynamic Tip Streaming from a Thin Disc, Phys. Rev. Lett. **126**, 064502 (2021).

[47] Y. Tian, Y. Liu, Z. Peng, C. Xu, D. Ye, Y. Guan, X. Zhou, W. Deng, and Y. Huang, Air entrapment of a neutral drop impacting onto a flat solid surface in electric fields, J. Fluid Mech. **946**, A21 (2022).

[48] Y. Tian, H. Wang, X. Zhou, Z. Xie, X. Zhu, R. Chen, Y. Ding, and Q. Liao, How does the electric field make a droplet exhibit the ejection and rebound behaviour on a superhydrophobic surface?, J. Fluid Mech. **941**, A18 (2022).

[49] D. A. Saville, Electrohydrodynamics: The taylor-melcher leaky dielectric model, Annu. Rev. Fluid Mech. **29**, 27 (1997).

[50] Y. Guan, S. Wu, M. Wang, Y. Tian, W. Lai, and Y. Huang, Numerical analysis of electrohydrodynamic jet printing under constant and step change of electric voltages, Phys. Fluids **34**, 062005 (2022).

[51] M. A. Herrada, J. M. Lopez-Herrera, A. M. Ganan-Calvo, E. J. Vega, J. M. Montanero, and S. Popinet, Numerical simulation of electrospray in the cone-jet mode, Phys. Rev. E **86**, 026305 (2012).

[52] I. Roghair, M. Musterd, D. van den Ende, C. Kleijn, M. Kreutzer, and F. Mugele, A numerical technique to simulate display pixels based on electrowetting, Microfluid Nanofluid **19**, 465 (2015).

[53] A. Russo, M. Icardi, M. Elsharkawy, D. Ceglia, P. Asinari, and C. M. Megaridis, Numerical simulation of droplet impact on wettability-patterned surfaces, Phys. Rev. Fluids **5**, 074002 (2020).

[54] Y. Guan, S. Wu, M. Wang, Y. Tian, C. Yu, W. Lai, and Y. Huang, Numerical investigation of high-frequency pulsating electrohydrodynamic jet at low electric bond numbers, Phys. Fluids **34**, 012001 (2022).

[55] J. H. Snoeijer and B. Andreotti, Moving contact lines: Scales, regimes, and dynamical transitions, Annu. Rev. Fluid Mech. **45**, 269 (2013).

[56] R. L. Grimm and J. L. Beauchamp, Dynamics of field-induced droplet ionization: Time-resolved studies of distortion, jetting, and progeny formation from charged and neutral methanol droplets exposed to strong electric fields, J. Phys. Chem. B **109**, 8244 (2005).

[57] O. A. Basaran and L. E. Scriven, Axisymmetric shapes and stability of charged drops in an external electric-field, Phys. Fluids **1**, 799 (1989).

[58] D. Bartolo, C. Josserand, and D. Bonn, Singular Jets and Bubbles in Drop Impact, Phys. Rev. Lett. **96**, 124501 (2006).

[59] G. I. Taylor, Studies in electrohydrodynamics. I. The circulation produced in a drop by electrical field, Proc. Math. Phys. Eng. Sci. **291**, 159 (1966).

[60] J. W. Ha and S. M. Yang, Deformation and breakup of newtonian and non-newtonian conducting drops in an electric field, J. Fluid Mech. **405**, 131 (2000).

[61] P. D. Hicks, E. V. Ermanyuk, N. V. Gavrilov, and R. Purvis, Air trapping at impact of a rigid sphere onto a liquid, J. Fluid Mech. **695**, 310 (2012).

[62] M. Pasandideh-Fard, Y. M. Qiao, S. Chandra, and J. Mostaghimi, Capillary effects during droplet impact on a solid surface, Phys. Fluids **8**, 650 (1996).

[63] S. Lin, D. Wang, L. Zhang, Y. Jin, Z. Li, E. Bonaccurso, Z. You, X. Deng, and L. Chen, Macrodrop-impact-mediated fluid microdispensing, Adv. Sci. **8**, 2101331 (2021).

[64] C. Stamatopoulos, P. Bleuler, M. Pfeiffer, S. Hedtke, P. R. von Rohr, and C. M. Franck, Influence of surface wettability on discharges from water drops in electric fields, Langmuir **35**, 4876 (2019).

[65] Q. Dong and A. Sau, Breakup of a leaky dielectric drop in a uniform electric field, Phys. Rev. E **99**, 043106 (2019).

[66] B. Sarma, S. Kumar, A. Dalal, D. N. Basu, and D. Bandyopadhyay, Electric-Discharge-Mediated Jetting, Crowning, Bursting, and Atomization of a Droplet, Phys. Rev. Appl. **15**, 014005 (2021).

[67] J. M. Lowe, V. Hinrichsen, I. V. Roisman, and C. Tropea, Impact of electric charge and motion of water drops on the inception field strength of partial discharges, Phys. Rev. E **102**, 063101 (2020).